

Supplementary Materials

High-performance room-temperature sodium-sulfur battery enabled by electrocatalytic sodium polysulfides full conversion

Nana Wang,^{ab} Yunxiao Wang,^a Zhongchao Bai,^b Zhiwei Fang,^b Xiao Zhang,^b Zhongfei Xu,^a Yu Ding,^b Xun Xu,^{a} Yi Du,^a Shixue Dou,^{a*} Guihua Yu^{b*}*

^a Institute for Superconducting and Electronic Materials, University of Wollongong,
Innovation Campus, Squires Way, Wollongong, New South Wales 2500, Australia

^b Materials Science and Engineering Program and Department of Mechanical
Engineering, The University of Texas at Austin, Austin, Texas 78712, United States

Experimental Procedures

MnCO₃ microsphere synthesis: MnSO₄·H₂O (2.366 g) was dissolved in a mixture of ethanol (98 mL) and deionized water (980 mL). Simultaneously, NH₄HCO₃ (11.06 g) was dissolved in deionized water (980 mL), and then was quickly added to the above prepared MnSO₄ solution under stirring. The mixture was just maintained overnight without stirring. The resultant light pink precipitation was filtered and collected to obtain MnCO₃ microspheres.

Carbon microsphere synthesis: The obtained MnCO₃ microspheres were heated at 550 °C under Ar atmosphere for 1 h with a heating rate of 2 °C min⁻¹. Afterwards, 0.4 g of the obtained Mn₂O₃ microspheres were dispersed ultrasonically in deionized water. Then, melamine (0.08 g), resorcinol (0.166 g), ethanol (11.6 ml), and ammonium hydroxide (0.066 mL) were added to the resultant dispersion. The mixture was kept under stirring for 30 min at 40 °C. After that, 0.4 ml of formaldehyde was added to above solution dropwise, with continuous stirring for 6 h at 40 °C. The obtained mixture was centrifuged at a low speed to collect the precipitated Mn₂O₃@C microspheres. The Mn₂O₃@C microspheres were heat-treated at 650 °C under Ar atmosphere with a heating rate of 2 °C min⁻¹ to form MnO with an activated carbon layer coating. Finally, the MnO@C microspheres were treated with dilute hydrochloric acid solution to remove MnO core, and carbon microspheres were left.

Carbon microspheres loaded with gold nanoparticles and sulfur: 15 mg of the above obtained carbon microspheres and 40 µL of HAuCl₄ 1 wt. % aqueous solution were dispersed in 8 mL of ethanol under stirring for 45 min. Simultaneously, 4 mg of NaBH₄ was dissolved in a mixture of 4 mL of ethanol and 4 mL of water. Then, after centrifugation of the carbon microspheres with HAuCl₄, the obtained NaBH₄ solution was added to the sediment under stirring in an ice water bath for 15 min. The carbon microspheres loaded with gold nanoparticles were collected after washing with ethanol and drying at 60 °C. For sulfur loading, 20 mg of carbon microspheres with encapsulated gold nanoparticles and 80 mg of sulfur powder were sealed in a tube and heated at 155 °C for 12 h, and then at 350 °C for 2 h.

Materials Characterization: The composition of the samples was investigated on a GBC MMA X-ray diffractometer (XRD, Cu K α radiation) instrument. The sulfur content was conducted on a Mettler-Toledo TGA/DSC1 Star System from 50 to 900 °C. The valence states of the elements were analyzed by X-ray photoelectron spectroscopy (XPS). The specific surface area and porosities of samples were collected

on a Micromeritics Tristar ii 3020 analyzer. The morphologies of the products were detected using field-emission scanning electron microscopy (FESEM, JEOL JSM-7500FA), transmission electron microscopy (TEM, JEOL 2011), and scanning transmission electron microscopy (STEM, JEOL ARM-200F).

Electrochemical measurements: The active materials, Super P, and carboxymethyl cellulose (CMC) binder were mixed in a mass ratio of 7: 2: 1, and then a few drops of water were added to them to form a uniform slurry. The thus-formed slurry was evenly coated on aluminum foil using a doctor blade and then dried in a vacuum oven for 12 h at 50 °C. The Al foil was punched into small rounds for use as cathodes, while the sodium metal served as the anode and glass fiber (Sigma-Aldrich, F6911-100EA) served as the separator. The electrolyte was 1.0 M NaClO₄ dissolved in propylene carbonate (PC) with 5 wt. % fluoroethylene carbonate (FEC) additive. The coin-type 2032 cells were assembled in an argon-filled glove box and tested on a LAND Battery tester at 25 °C in the voltage range from 0.8 to 2.8 V. The cyclic voltammograms and electrochemical impedance spectra (EIS) were collected on a Biologic VMP-3 electrochemical instrument. The coin-type 2032 cells were used for *in-situ* synchrotron XRD characterization, with two holes punched on both sides of the cell.

Calculation method: All density functional theory (DFT) calculations were performed using the Vienna Ab Initio Simulation Package (VASP). The generalized gradient approximation (GGA) was applied to treat the exchange correlation energy with the Perdew-Burke-Ernzerhof (PBE) functional. The projector augmented wave (PAW) method was employed to describe electron-ion interactions, with the cut-off energy of 400 eV. A 30 Å × 30 Å × 30 Å supercell was constructed, and N-doped carbon with 60 C atoms was modeled with edge-hydrogenated graphene, which was located in the center of the supercell. Adsorbed Au structures were built from clusters of four Au atoms added on to the N-doped carbon. All structures in the calculations were relaxed until the convergence tolerance of the force on each atom was smaller than 0.02 eV. The energy convergence criterion was set to be 1 × 10⁻⁴ eV for self-consistent calculations, and k-point sampling was restricted to the Gamma point only. The Gibbs free energy of conversion ΔG was calculated by the following equation,

$$\Delta G = (\Delta G_{\text{Na}_x\text{S}_y} - xG_{\text{Na}} - y/8G_{\text{S}_8}) / (x + y)$$

where $\Delta G_{\text{Na}_x\text{S}_y}$ is the Gibbs free energy of molecules Na_xS_y. G_{Na} and G_{S_8} are the energy per atom of Na and S in the solid sodium and S₈ molecules, respectively.

S1. Phase and morphology characterization of MnCO₃ spheres.

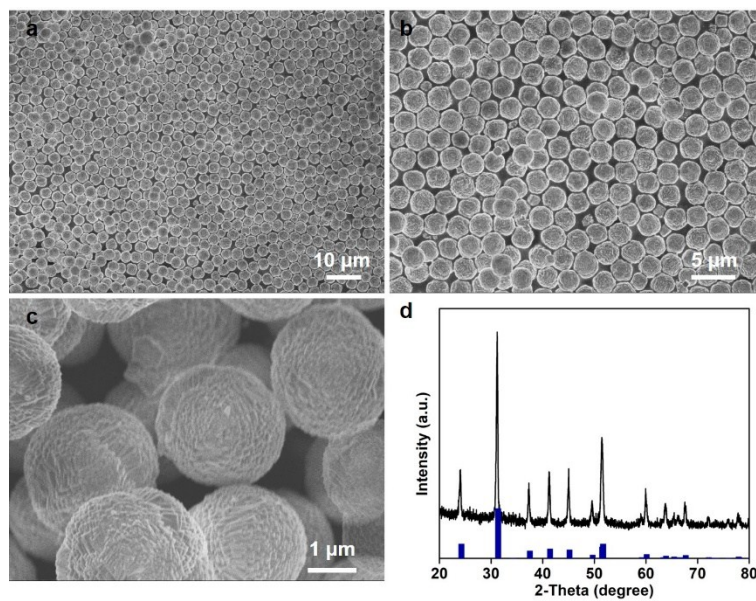


Fig. S1. (a-c) SEM images and (d) XRD pattern of MnCO₃ (JCPDF Card no. 44-1472).

S2. Phase and morphology characterization of Mn_2O_3 spheres.

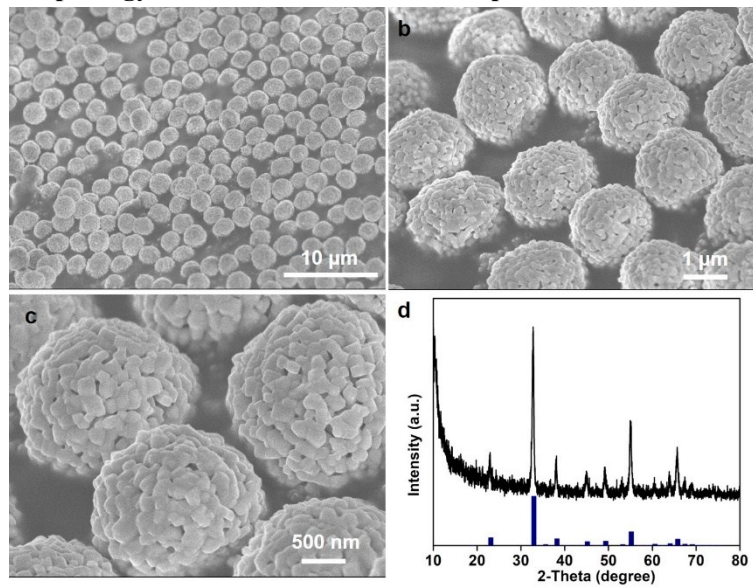


Fig. S2. (a-c) SEM images and (d) XRD pattern of Mn_2O_3 (JCPDF Card no. 41-1442).

S3. Phase and morphology characterization of MnO@N-C spheres.

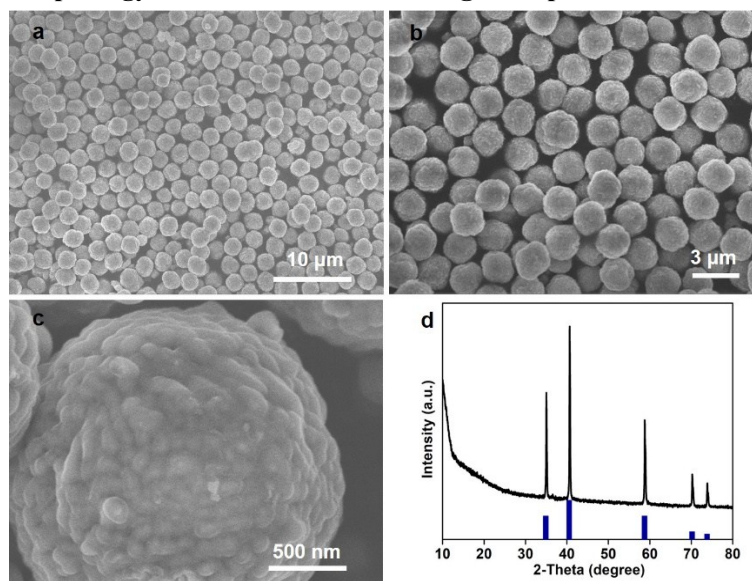


Fig. S3. (a-c) SEM images and (d) XRD pattern of MnO@N-C (JCPDF Card no. 07-0230).

S4. Phase and morphology characterization of N-doped carbon microspheres.

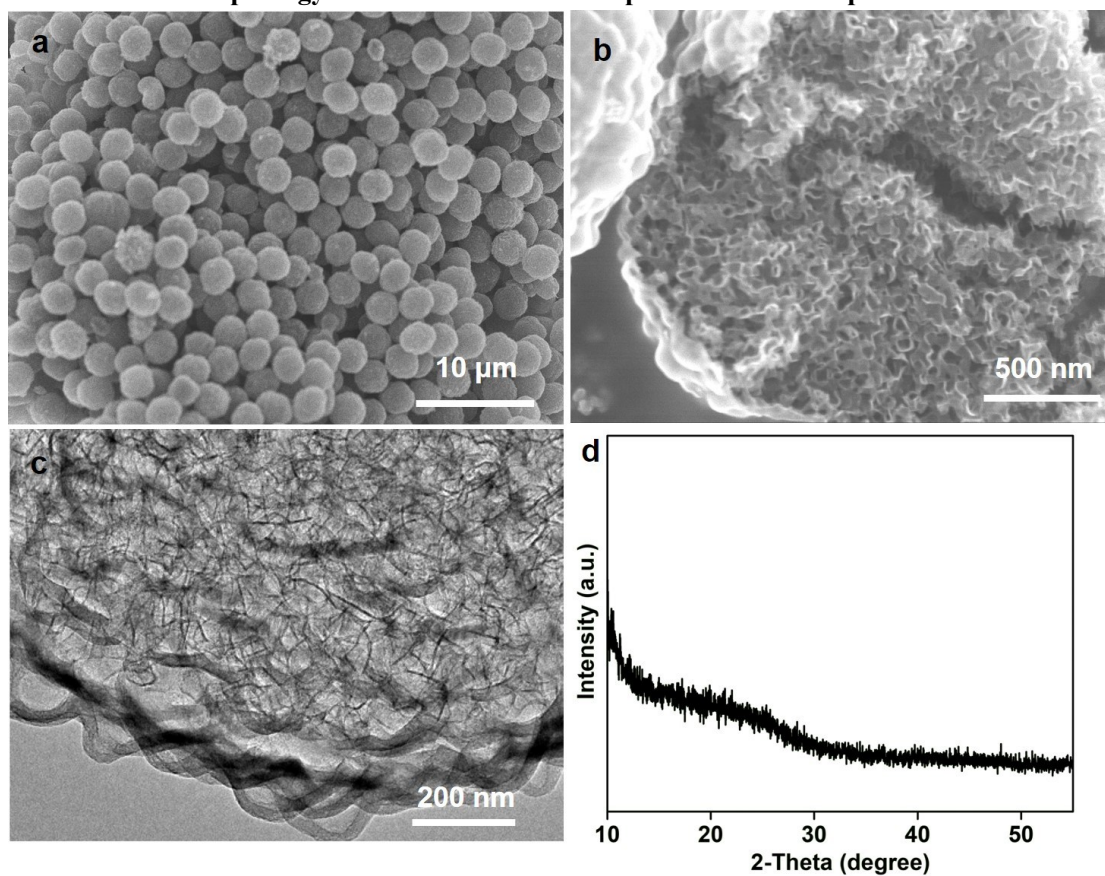


Fig. S4. (a, b) SEM images, (c) TEM image, and (d) XRD pattern of N-doped carbon microspheres after treatment with HCl solution.

S5. Morphology characterization of CN/Au sample.

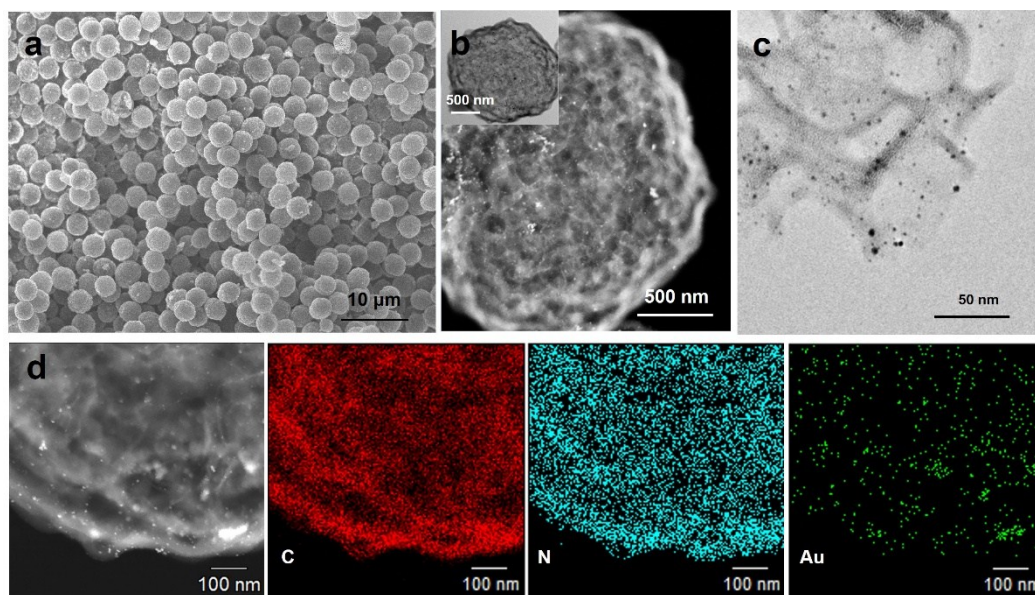


Fig. S5. (a) SEM image, (b) dark-field TEM image, with the inset showing lower resolution, (c) STEM image and (d) dark-field TEM image and corresponding elemental mapping images of the CN/Au sample.

S6. XRD pattern of CN/S sample.

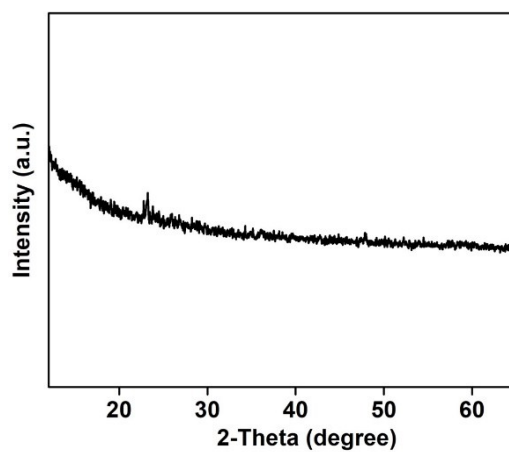


Fig. S6. XRD pattern of the sulfur loaded CN (CN/S) sample.

S7. XPS analysis of CN sample.

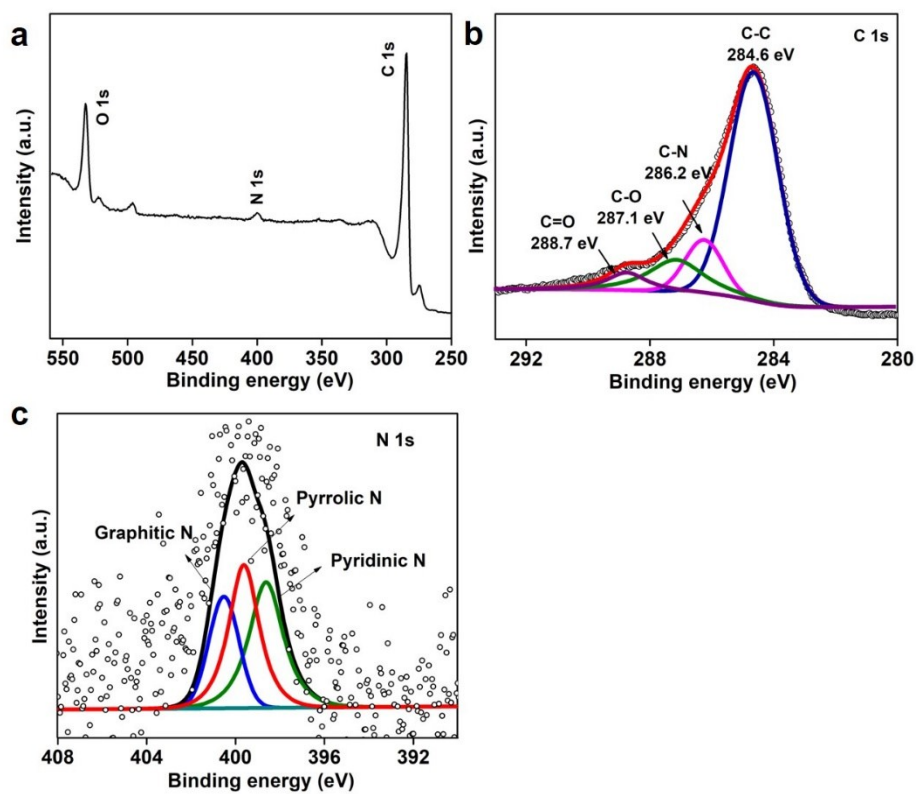


Fig. S7. (a) XPS survey spectrum (a), and high resolution XPS spectra of (b) C 1s and (c) N 1s for the CN sample.

S8. XPS analysis of CN/Au/S sample.

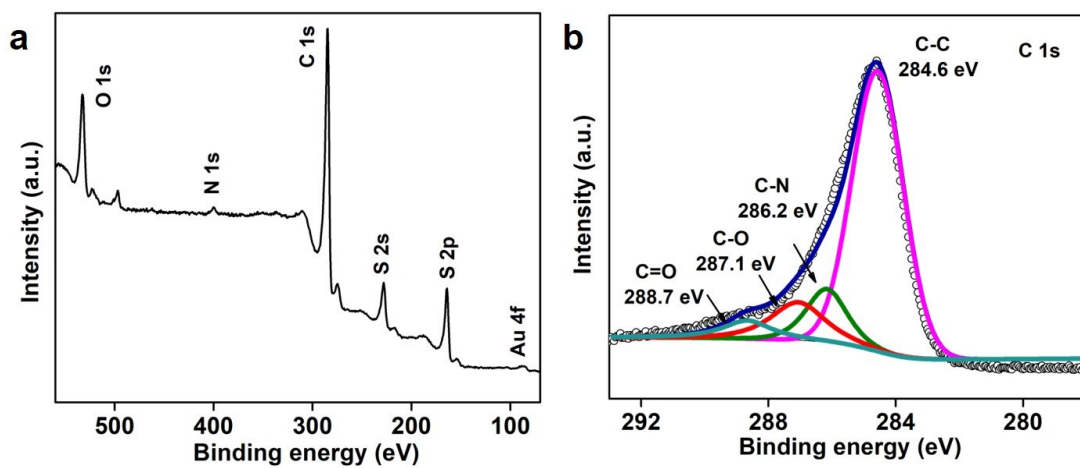


Fig. S8. XPS survey spectrum (a) and high resolution XPS spectrum (b) of C 1s for the CN/Au/S sample.

S9. XPS analysis of CN/Au sample.

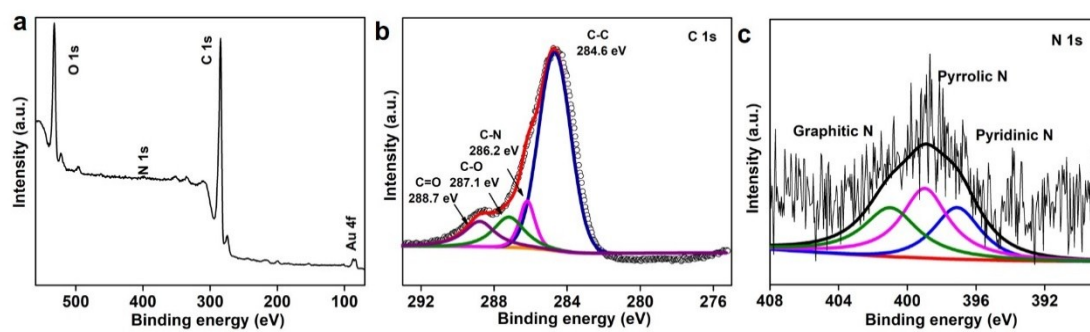


Fig. S9. XPS survey spectrum (a), and high resolution XPS spectra of (b) C 1s and (c) N 1s for the CN/Au sample.

S10. *Ex situ* XRD patterns of CN/S and CN/Au/S samples during cycling.

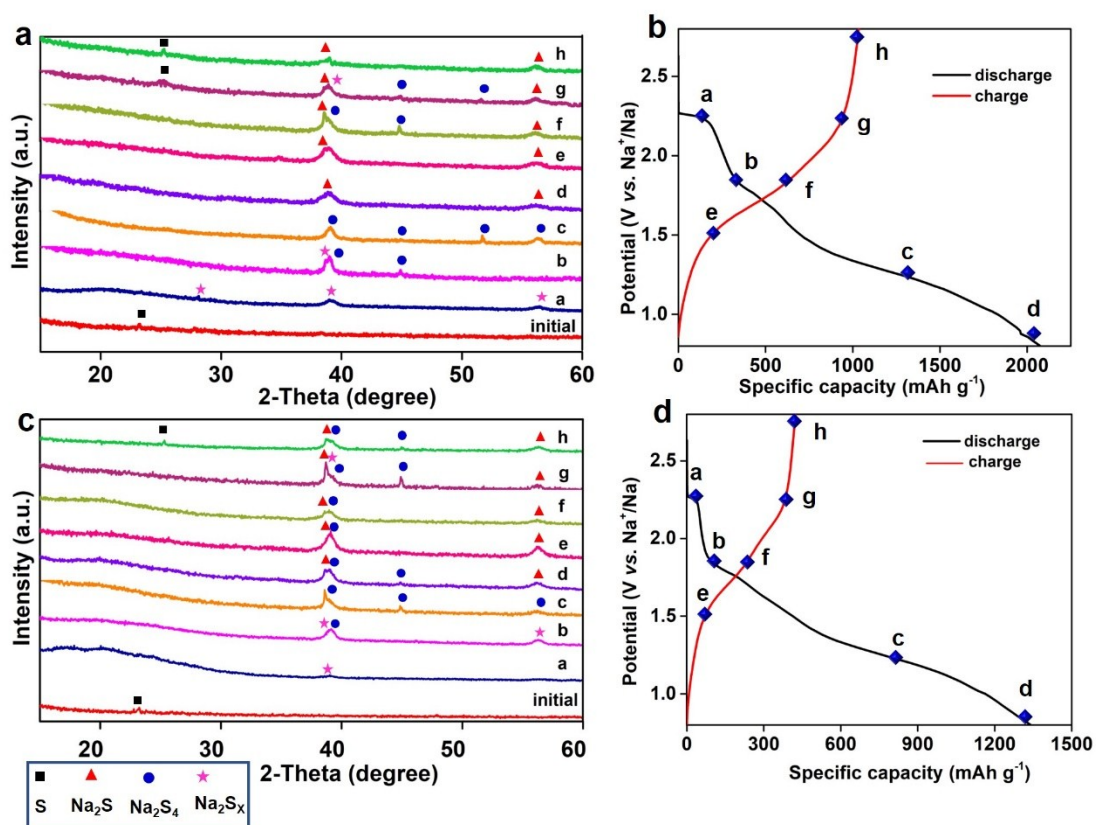


Fig. S10. (a) *Ex situ* XRD patterns for charged and discharged CN/Au/S sample. (b) Charge and discharge curves for CN/Au/S sample. (c) *Ex situ* XRD patterns for charged and discharged CN/S sample. (d) Charge and discharge curves for CN/S sample. (a: 2.2 V; b: 1.8 V; c: 1.2 V; d: 0.8 V; e: 1.5 V; f: 1.8 V; g: 2.2 V; h: 2.8 V).

S11. CV curves for CN/Au/S and CN/S samples.

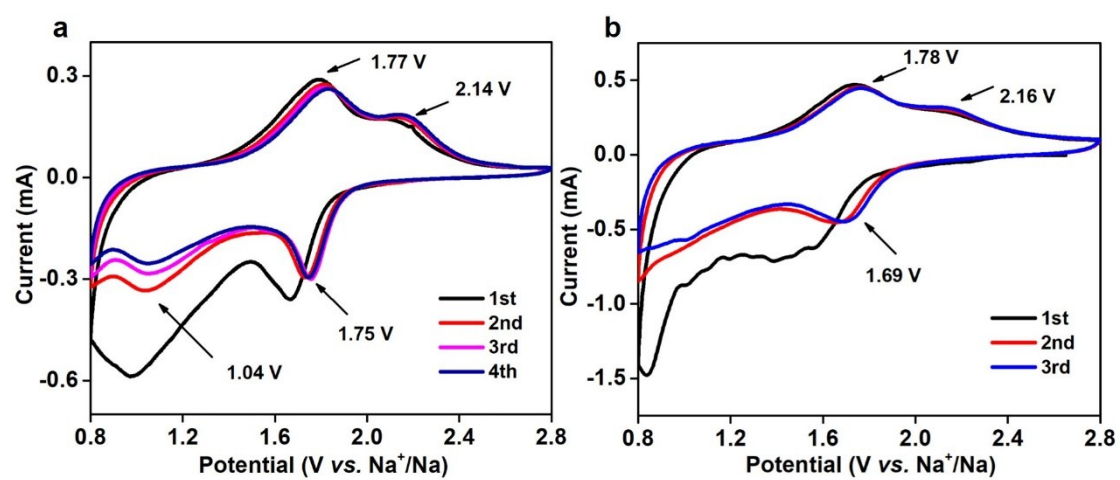


Fig. S11. CV curves for (a) CN/Au/S and (b) CN/S samples.

S12. Electrochemical performance of N-doped carbon microspheres.

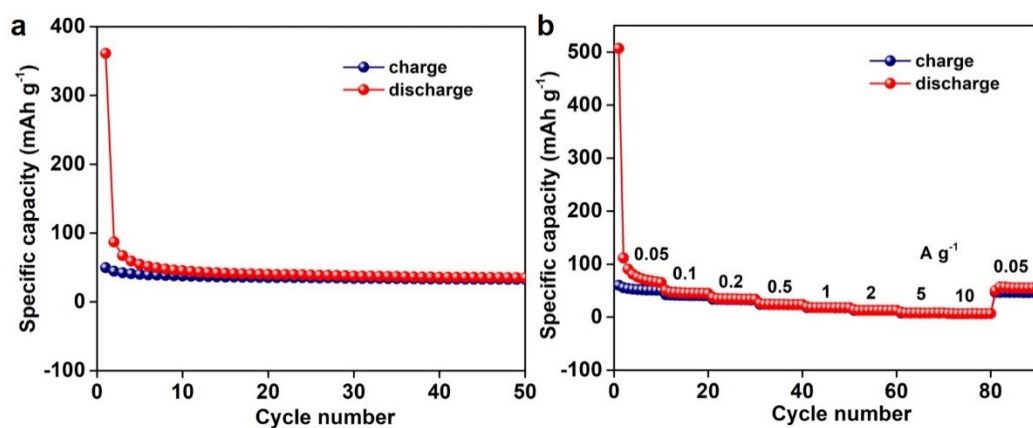


Fig. S12. (a) Cycling performance at a current density of 100 mA g⁻¹, and (b) rate performance of N-doped carbon microspheres in the voltage range of 0.8 to 2.8 V.

Note: The initial discharge and charge capacity for CN microspheres is 361 and 50 mAh g⁻¹, respectively, with a coulombic efficiency of 13.85%, due to the solid electrolyte interphase (SEI) formation because of the high specific surface area. The CN microspheres deliver reversible capacities of 32 mAh g⁻¹ at a current density of 100 mA g⁻¹. Thus, the capacity contribution of CN microspheres could be ignored in the CN/Au/S system.

S13. Electrochemical performance of CN/Au/S sample.

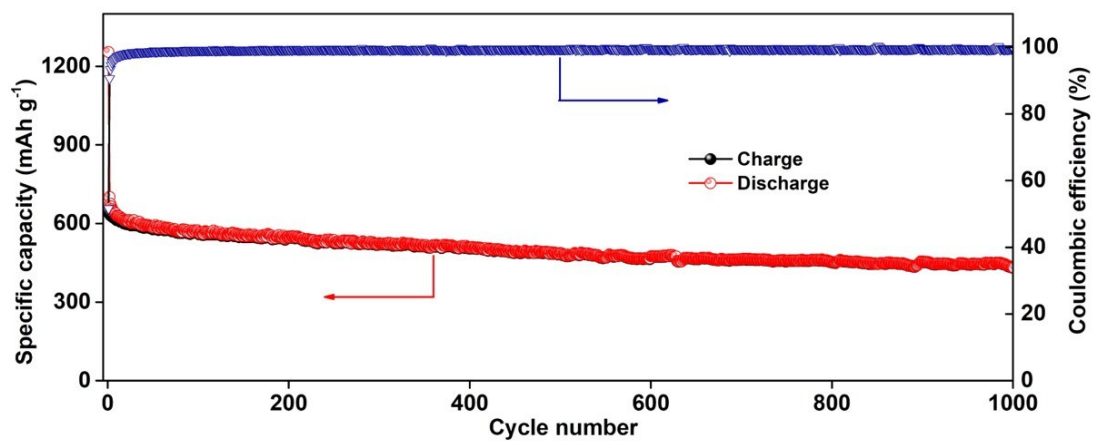


Fig. S13. Long-term cycling stability of CN/Au/S sample at a current density of 2 A g⁻¹.

S14. stability of the gold nanodot during cycling.

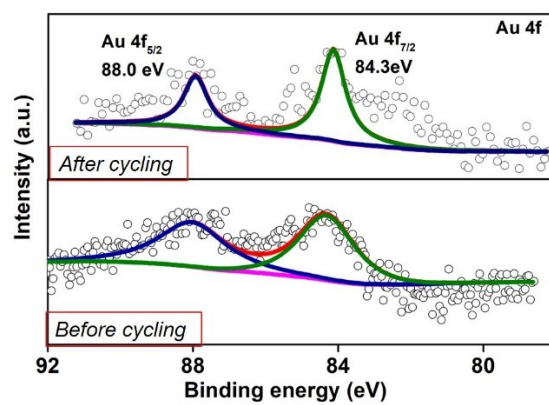


Fig. S14. XPS spectra of Au 4f for the CN/Au/S sample after 100 cycles at a current density of 0.1 A g⁻¹.

S15. EIS spectra of CN/S and CN/Au/S sample.

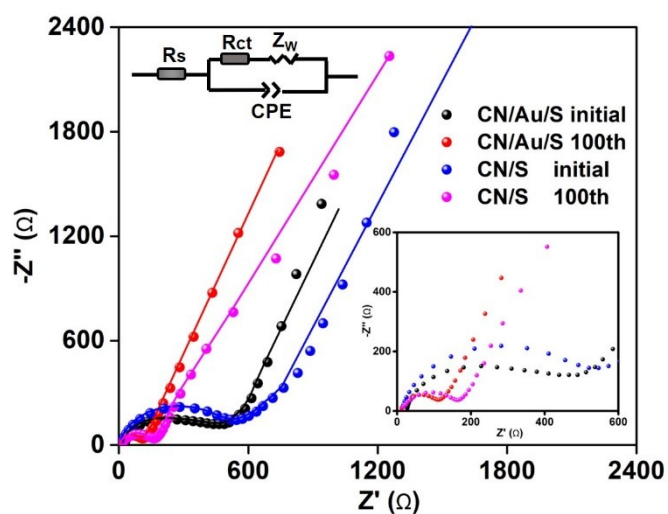


Fig. S15. Nyquist plots of CN/S and CN/Au/S samples were collected from 100 kHz to 1Hz in the initial state and after 100 cycles. The inset is the equivalent circuit and an enlargement of the high frequency region.

Note: The electrochemical impedance spectroscopy (EIS) plot is composed of a sloping line in the low frequency region that is related to the Warburg diffusion process and one depressed semicircle in the high frequency region corresponding to the charge-transfer resistance (R_{ct}).

S16. CV curves of CN/S sample.

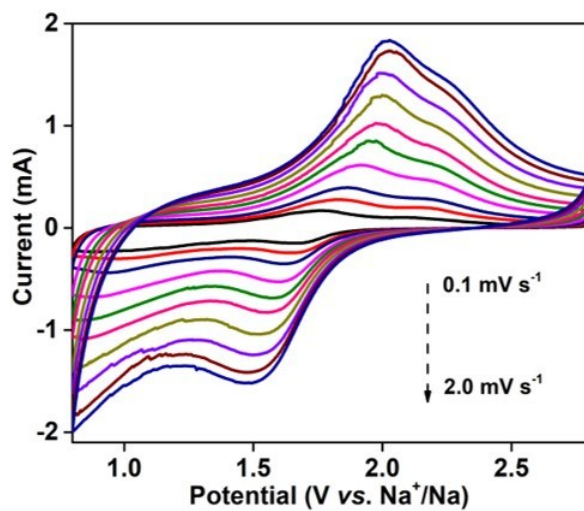


Fig. S16. CV curves of CN/S sample from 0.1 to 2.0 mV s^{-1} .

S17. Charge-discharge curves of CN/S sample.

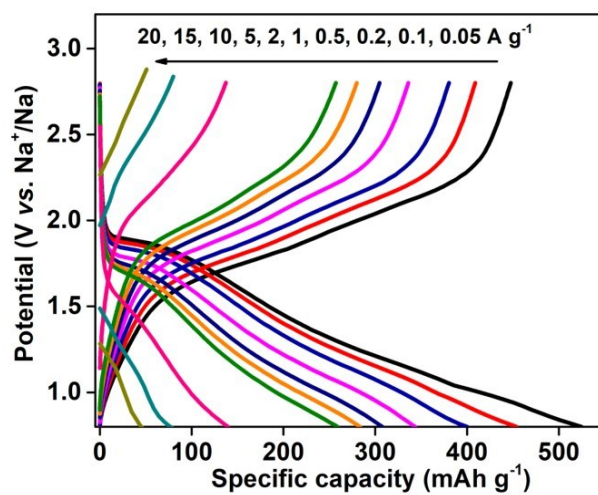


Fig. S17. Charge-discharge curves at various current densities for the CN/S sample.

Table S1. The electrochemical performance comparison between S-based cathodes from references and CN/Au/S sample in this work.

| Material | Voltage [V] | Sulfur content | Cycling mAh/g (mA/g), cycle number | Rate Capacity mAh/g (current density mA/g) | Ref. |
|--|-------------|----------------|--|---|-----------|
| S@Fe-HC | 0.8-2.8 | 40% | 394 (0.1), 1000 th | -- | 1 |
| NiS ₂ @NPC Ts/S | 0.8-2.8 | 56% | 401 (1), 750 th | 760 (0.1), 691 (0.2), 557 (0.5), 457 (1), 346 (2), 203 (5) | 2 |
| SC-BDSA | 0.6-2.8 | 40.07% | 750 (0.25), 200 th 452 (2.5), 1000 th | 903 (0.5), 741 (2), 526 (8), | 3 |
| (C/S/BaTiO ₃)@TiO ₂ | 0.5-2.7 | 60% | 611 (0.5), 400 th | 671 (0.1), 622.5 (0.5), 518 (1), 415 (1.5), 350 (2) | 4 |
| S@Con-HC | 0.8-2.8 | 47% | 508 (0.1), 600 th | 820 (0.1), 498 (0.2), 383 (0.5), 313 (1), 269 (2), 220 (5) | 5 |
| S _{0.6} Se _{0.4} /CN | 0.8-3.0 | -- | 375 (0.1), 100 th 202 (0.5), 160 th | 374 (0.1), 290 (0.2), 202 (0.5), 117 (1.0), | 6 |
| S@C | 0.8-2.6 | -- | 410 (0.167), 250 th 306 (1.67), 1500 th , | 370 (1.67) | 7 |
| S@iMCHS | 0.8-2.8 | 59.4% | 292 (0.1), 200 th | 391 (0.1), 386 (0.2), 352 (0.5), 305 (1), 174 (2), 127 (5) | 8 |
| HSMC-Cu-S | 0.8-2.6 | 50% | 610 (0.05), 110 th | 350 (2.01), ~100 (5.02) | 9 |
| CN/Au/S | 0.8-2.8 | 56.5% | 430 (2), 1000 th 369 (10), 2000 th | 1010 (0.05), 830 (0.1), 755 (0.2), 678 (0.5), 599 (1), 532 (2), 414 (5), 297 (10), 230 (15), 181 (20) | This work |

It is notable that the sulfur content and its working voltage both would influence the cycling and rate performance of RT-Na/S batteries. The lower sulfur content is beneficial for the sulfur utilization but would reduce the volume and mass energy density of whole electrodes. Meanwhile, the lower voltage window would increase the mass specific capacity reduce the output energy density of RT-Na/S batteries. In high output voltage and high sulfur content, CN/Au/S sample in our work presents very good performance under the same test condition.

Reference:

1. B. W. Zhang, T. Sheng, Y.-X. Wang, S. L. Chou, K. Davey, S.-X. Dou, S.-Z. Qiao, *Angew. Chem.* **2019**, *131*, 1498.
2. Z. Yan, J. Xiao, W. Lai, L. Wang, F. Gebert, Y. Wang, Q. Gu, H. Liu, S.-L. Chou, H. Liu, S.-X. Dou, *Nat. Commun.* **2019**, *10*, 4793.
3. T. Wu, M. Jing, L. Yang, G. Zou, H. Hou, Y. Zhang, Y. Zhang, X. Cao, X. Ji, *Adv. Energy Mater.* **2019**, *9*, 1803478
4. D. Ma, Y. Li, J. Yang, H. Mi, S. Luo, L. Deng, C. Yan, M. Rauf, P. Zhang, X. Sun, X. Ren, J. Li, H. Zhang, *Adv. Funct. Mater.* **2018**, *28*, 1705537.
5. B.-W. Zhang, T. Sheng, Y.-D. Liu, Y.-X. Wang, L. Zhang, W. Lai, L. Wang, J. Yang, Q.-F. Gu,

- S.-L. Chou, H.-K. Liu, S.-X. Dou, *Nat. Commun.*, **2018**, *9*, 4082.
6. Y. Yao, L. Zeng, S. Hu, Y. Jiang, B. Yuan, Y. Yu, *Small*, **2017**, *13*, 1603513.
 7. R. Carter, L. Oakes, A. Douglas, N. Muralidharan, A. P. Cohn, C. L. Pint, *Nano Lett.*, **2017**, *17*, 1863.
 8. Y.-X. Wang, J. Yang, W. Lai, S. L. Chou, Q.-F. Gu, H. K. Liu, D. Zhao, S. X. Dou, *J. Am. Chem. Soc.* **2016**, *138*, 16576
 9. S. Zheng, P. Han, P. Li, H. Zhang, J. Yang, *Adv. Energy Mater.*, **2014**, *4*, 1400226